

Mass Partitioning in Fragmenting Tin Sheets

Bo Liu^{1,2}, Randy A. Meijer¹, Wei Li¹, Javier Hernandez-Rueda^{1,†}, Hanneke Gelderblom³,
and Oscar O. Versolato^{1,2,*}

¹*Advanced Research Center for Nanolithography (ARCNL), Science Park 106, Amsterdam 1098 XG, Netherlands*

²*Department of Physics and Astronomy, and LaserLaB, Vrije Universiteit Amsterdam, De Boelelaan 1081, Amsterdam 1081 HV, Netherlands*

³*Institute for Complex Molecular Systems and J. M. Burgers Center for Fluid Dynamics, Department of Applied Physics, Eindhoven University of Technology, Den Dolech 2, Eindhoven 5600 MB, Netherlands*

 (Received 3 April 2023; revised 5 June 2023; accepted 23 June 2023; published 21 July 2023)

We experimentally study the mass partitioning of a fragmenting liquid sheet formed after the impact of a ns-laser pulse on a tin microdroplet, and its dependence on laser pulse energy and droplet size. We present the temporal evolution of individual liquid fractions: the sheet and its bounding rim, ligaments protruding from the rim, and droplets shed by the ligaments, applying machine learning to analyze sub-resolution fragments. Our results show that the temporal evolution of the mass partitioning between the sheet, rim, ligaments, and fragments is independent of the deformation Weber number—following Wang and Bourouiba [J. Fluid Mech. **935**, A29 (2022)] for the analogous droplet-pillar impact case, extending the work to larger Weber numbers and to a system where the timescale of deformation is fully decoupled from impact. The full mass partitioning is accounted for by quantifying the further contributions unique to the laser-droplet impact case: that of a centrally located mass remnant, and the mass ablated by the laser pulse. These findings can be employed to optimize the mass utilization of the liquid tin that is used as target material in the production of extreme ultraviolet light for nanolithography.

DOI: [10.1103/PhysRevApplied.20.014048](https://doi.org/10.1103/PhysRevApplied.20.014048)

I. INTRODUCTION

State-of-the-art extreme ultraviolet (EUV) sources for nanolithography generate EUV light from laser-produced plasma fed with liquid tin microdroplets irradiated by high-energy laser pulses [1–5]. EUV lithography enables the production of the most advanced semiconductor devices and is critically dependent on the production of EUV light. EUV light is generated in a two-step process, in which a first laser *prepulse* is employed to shape the initial spherical droplet into a pizza shape: a thin axisymmetric sheet with a thickness of just several tens of nanometers and a thick bounding rim with a diameter of several micrometers [6,7]. In a single lithography machine, this process is repeated at an approximately 50-kHz rate—thus firing on a trillion droplets over a year of operation. At the bounding

rim, ligaments protrude radially outward; the ligaments, in turn, shed droplets [8,9]. This complex liquid “target” further interacts with a second laser pulse. This *main pulse* turns the liquid tin into a plasma that emits EUV radiation with a wavelength centered around 13.5 nm [10–13]. Undoubtedly, the local liquid-mass distribution of the tin target heavily influences its response to a subsequent laser pulse. Furthermore, the shed droplets may carry a considerable amount of tin from the liquid system away from the laser interaction zone, contributing to the risk of contaminating nearby light-collecting optics with tin “debris.” A deeper understanding of the temporal and spatial evolution of the liquid mass of the prepulse-shaped targets is valuable for further optimization of EUV light sources to increase EUV output power and to minimize the tin-mass consumption and generation of tin debris.

The fluid dynamic response of a tin microdroplet to a laser-pulse impact resembles the ubiquitous cases of water droplets impinging on solids, see, e.g., Refs. [6,8,9,14–26]. Wang and Bourouiba [27] elucidated in detail the mass partitioning in the sheet, bounding rim, ligaments, and fragments produced from droplet-pillar impact. It was found that the mass fractions contained in these channels are independent of the impact conditions (captured by the Weber number) and can be described as a sole function of time. Despite the similarity to its mechanical counterpart

*o.versolato@arcnl.nl

†Current address: Department of Optics, Faculty of Physical Sciences, Complutense University of Madrid, Plaza de Ciencias 1, 28040 Madrid, Spain.

Published by the American Physical Society under the terms of the [Creative Commons Attribution 4.0 International](https://creativecommons.org/licenses/by/4.0/) license. Further distribution of this work must maintain attribution to the author(s) and the published article's title, journal citation, and DOI.

of droplet impact onto an obstacle, laser-pulse impact onto a droplet does provide some key insights into the droplet dynamics. First, during laser-pulse impact, the timescales of impact and droplet deformation are completely decoupled, which allows investigation of the late-time fluid dynamic response to perturbations caused by the early time laser pulse [14,28]. Second, laser impact provides access to much larger Weber numbers, which enables us to significantly extend the range of investigation and test the robustness of scaling relations. Inspired by Ref. [27], we propose that the initial volume of a laser-impacted droplet $V_0 = \pi D_0^3/6$ (with a diameter of D_0) is distributed over a *sheet*, a bounding *rim*, *ligaments* that radially protrude from this rim, and *fragments* generated by the breakup of ligaments. One further feature, unique to the laser-droplet impact case, is the presence of a *center mass*—a disk located in the center of the sheet [6,7]. Apart from these channels, a certain *ablated mass* fraction of tin will be heated up by the laser pulse and converted to a plasma or vapor phase, propelling the droplet and setting the impact conditions [28–30]. The mass distribution of the tin from the initial droplet is thus given by

$$V_0 = V_s + V_r + V_l + V_f + V_c + V_a, \quad (1)$$

where the volume—or, equivalently, mass—in the sheet, rim, ligaments, fragments, center mass, and the mass ablated by the laser pulse are represented by V_s , V_r , V_l , V_f , V_c , and V_a , respectively.

Several studies have been carried out to better understand the dynamics of the various contributions to Eq. (1). However, so far only the contribution of V_s was explicitly experimentally quantified [6,7]. Ligaments were investigated by Klein *et al.* [8] in terms of their number and the scaling thereof with the impact Weber number. The dynamics of tin-fragment shedding was experimentally investigated in Ref. [9], focusing on the speed of the fragments but leaving out information on the fragment-size distribution. Although the main channels for tin partitioning have thus been identified and studied individually, an explicit quantification of the volume fraction in the channels of V_r , V_f , V_l , V_c , and V_a has not yet been undertaken, and the validity, or rather the completeness of Eq. (1) remains unattested.

In this work, we present the global volume partitioning among the channels listed in Eq. (1) by combining our experimental results on droplet-laser impact with existing analytical models developed for the similar case of a droplet impacting a pillar extending the range to much larger Weber numbers (from the approximately 300–900 range of Ref. [27] to approximately 1000–5500 in the current work), and using machine learning techniques. We present our results on the individual volume fractions taken

up by the various channels and thus provide the full volume distribution of tin in a target, and discuss application perspectives.

II. EXPERIMENTS AND METHODS

Our experimental setup is described in detail in Ref. [9]. Key aspects and related updates are summarized below [see Fig. 1(a)]. A vertically aligned train of liquid tin microdroplets (at 260°C, with density $\rho = 6960 \text{ kg/m}^3$, surface tension $\sigma = 0.54 \text{ N/m}$, and dynamic viscosity $\mu = 1.8 \times 10^{-3} \text{ Pa s}$ [31,32]) is dispensed by a droplet generator mounted on top of a vacuum vessel (10^{-7} mbar). In experiments, we systematically vary the diameter of droplets D_0 from 34 to 67 μm . The droplet train, traveling at a speed of approximately 10 m/s and a repetition rate ranging from 4 to 80 kHz, passes through a horizontal light sheet, which is generated by a helium-neon (He-Ne) laser and is positioned about 4 mm above the center of the vacuum vessel, i.e., the laser-droplet interaction point. The scattered He-Ne light is captured by a photomultiplier tube, from which the kilohertz-frequency signal is down-converted to a 10-Hz signal that serves as the trigger to the data acquisition and laser systems.

A circularly polarized laser beam generated from a Nd:YAG laser-pulse system operating at a wavelength of 1064 nm is aligned onto the droplets at the center of the vacuum vessel. The laser pulse has a Gaussian temporal shape and a duration of 10 ns at FWHM. The laser beam is focused down at the droplet location to a focal spot with a size of 110 μm at FWHM. The energy of the laser pulse is varied using a half-wave plate in series with a thin-film polarizer (cf. Fig. 1), which, together with the given range of droplet sizes, allows access to a Weber number range spanning approximately 1000–5500 in the current work.

The response of droplets is inspected using a stroboscopic shadowgraph imaging system. We record the expansion and fragmentation behavior of droplets by using two CCD cameras attached to long-distance microscopes (K2 DistaMax, Infinity Photo-Optical) at 90° and 30° with respect to the laser propagation direction, thus obtaining side- and front-view images, respectively. Both microscopes are equipped with a CF-3 objective (Infinity Photo-Optical) and are positioned at a distance of 110 mm to the center of the vessel. For the front view, we employ a double-frame camera (pco.4000), which is capable of capturing two consecutive frames of the same tin sheet with a minimum interframe time of approximately 280 ns. We use a single-frame camera (Manta G145-B, AVT) for the side view. The target is back lit by two consecutive and identical, incoherent light pulses with a wavelength of $560 \pm 10 \text{ nm}$ and pulse duration of 5 ns (FWHM). The first pulse is positioned within the exposure windows of both the Manta camera (side view) and the first frame of the pco camera (front view). The second illumination pulse, which

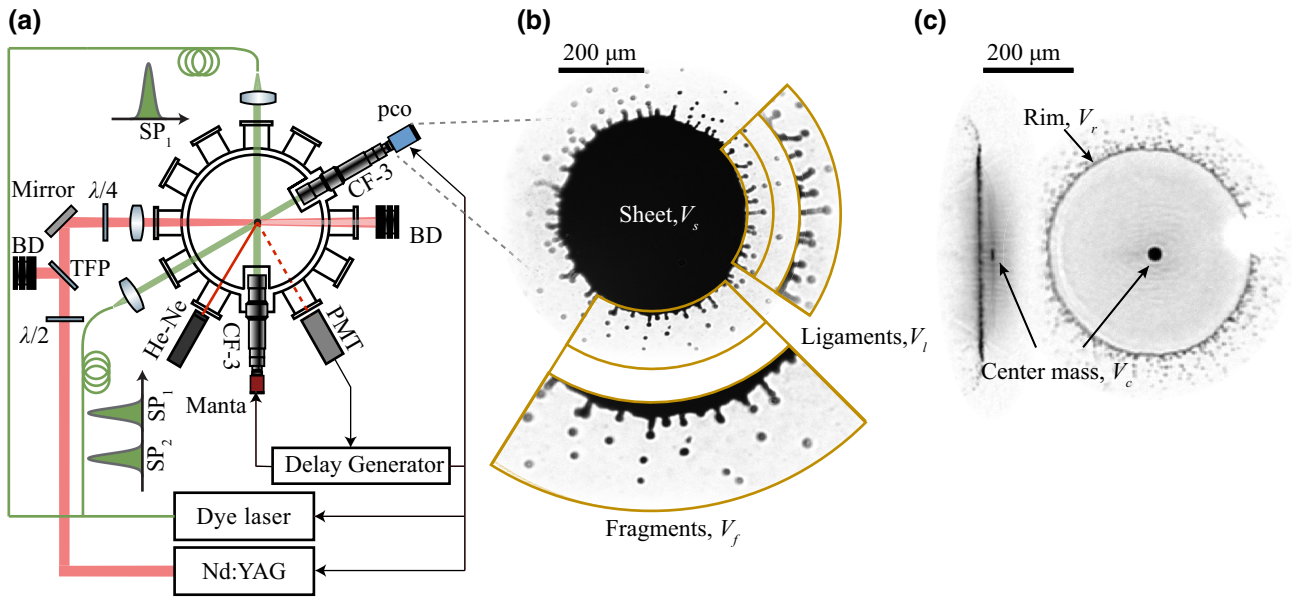


FIG. 1. (a) Top-view schematic of the experimental setup comprising a vacuum chamber, synchronization and trigger systems, Nd:YAG laser, and shadowgraphic imaging systems. The energy of the laser pulse is varied using a half-wave plate ($\lambda/2$) in series with a thin-film polarizer (TFP) and a beam dump (BD). A quarter-wave plate ($\lambda/4$) is used before the final focusing lens to set a circular polarization. The imaging systems provide front- (pco) and side-view (Manta) images of the expanding tin sheet using long-distance microscopes (see the main text). Two consecutive shadowgraphy probe pulses SP₁ and SP₂ are used as illumination sources for the front-view microscope, whereas a single pulse SP₁ is used for the side-view system. Figure adapted from Liu (2022) [9]. (b) A front-view shadowgraphy image showing a typical expanding sheet following the impact of a 20-mJ laser pulse on a droplet with an initial diameter of 67 μm . Insets provide an enlarged view of fragments and ligaments. (c) Side- and front-view shadowgraphy images of a liquid tin sheet after being irradiated with a 50-ns-length vaporization pulse (for details see Ref. [7]). The vaporization pulse removes the liquid from the thin sheet, enabling visualization of the relatively thick features, including the bounding rim and the center mass. The individual volumes contributing to Eq. (1) are indicated in (b),(c).

follows the first pulse with a tunable time delay (typically set from 1 to 5 μs in the experiment), is collected by the second-frame exposure window of the pco camera only.

Our dual-camera imaging system has been upgraded to provide improved resolution not only for the front-view [9], but also for the side-view camera. The images are used to determine the diameter of (subresolution) spherical fragments d_f through machine-learning techniques. Furthermore, by employing a double-frame camera, we obtain the detachment time t_d for each individual fragment according to the method described in Ref. [9]. Relating the detachment time of each fragment to its diameter provides the instantaneous size of the shed fragments $d_f(t_d)$. These results, in combination with the shedding rate (the rate of increase of the fragment number), yield the volume of liquid accumulated in the fragments V_f over time. Next, our postprocessing of the front-view images allows us to accurately detect the formation of ligaments at the edge of the sheet [see Fig. 1(b)]. By finding the position of the bounding rim, the length of each ligament L_l growing from the rim is determined. To obtain the instantaneous thickness of the ligaments w_l , we invoke analytical models from Refs. [16,33]. The data of w_l , L_l , and the ligament number N_l allow for a determination of the volume of ligaments V_l .

We obtain the volume of the center mass V_c [visualized in Fig. 1(c), see caption for details] by the associated remnant of liquid situated in the center of the sheet, as assessed from side-view images. By reviewing the experimentally validated numerical simulations performed in Ref. [30], originally designed to study the early time droplet deformation, we are able to estimate the volume of ablated material V_a . Next, we briefly recap the experimental study on the volume of the sheet V_s previously presented in Refs. [6,7]. We infer the volume of the rim V_r obtained by using our data of the radial location of the rim R_r in tandem with a robust analytical model from Ref. [33].

A. Assumptions

We note that our findings regarding the global mass distribution are based on the assumption that the density of liquid tin remains constant in our observation time regime (on the order of μs). To support this assumption, an extreme example case is investigated where a droplet with $D_0 = 30 \mu\text{m}$ is irradiated with a particularly energetic laser pulse with $E_p = 80 \text{ mJ}$, a beam diameter of 60 μm (flat-top), and a pulse duration of 20 ns (square) in a radiation-hydrodynamic simulation using RALEF-2D (see below).

At $t = 21$ ns (i.e., 1 ns after the laser is turned off), most of the liquid has a temperature < 1021 K (plasma shielding prevents laser light from directly heating the surface), at which the density of liquid tin is 6643 kg/m³, 4.6% less than the density at the initial liquid-tin temperature in our experiments (6960 kg/m³ at 533 K, cf. Sec. II) [31]; meanwhile the surface tension decreases by a similar 5.8% [32] and the ratio ρ/σ , which appears in the pertinent equations in the following, by just 1%. We also assume that the response of the droplet to a 10-ns-length (FWHM) laser pulse is dominated by incompressible flow. The validity of this assumption is supported by Ref. [30] where our results of kinetic energy partitioning were shown to agree with an analytical fluid-dynamic model developed by Gelderblom *et al.* [14] for an incompressible liquid droplet responding to an instantaneous pressure impulse. The assumption is further supported by the studies by Reijers *et al.* [34] and Meijer *et al.* [35], which conclude that an incompressible flow will dominate the droplet response when $\tau_p/\tau_a \gtrsim 1$ for a Gaussian-temporally-shaped pulse; $\tau_a = R_0/c_s$ is the acoustic time, which characterizes the acoustic wave that traverses the droplet at the speed of sound $c_s \approx 2500$ m/s [36]. In our case, the pulse duration satisfies $\tau_p \gtrsim \tau_a$. Still, we do find some compressibility effects as we hypothesize that the center-mass feature is a result of the collapse of a cavity generated by a rarefaction wave (cf. Sec. III B).

III. RESULTS

A. Volume of the fragments and ligaments

To obtain the volume of fragments and ligaments, we first need to assess their diameters. In addition, other parameters such as fragment number, ligament number, and ligament length are required to fully determine the volume of fragments and ligaments. In this section, we first discuss the temporal evolution of the volume accumulated in fragments V_f .

The volume accumulated in the fragments over time can be expressed as

$$V_f(t) = \int_{t_{\text{onset}}}^t \frac{\pi}{6} d_f^3 \dot{N}_f d\tilde{t}, \quad (2)$$

where t_{onset} is the onset time of fragmentation, \dot{N}_f the shedding rate related to the fragment number N_f , and d_f the diameter of the newly formed fragments. Equation (2) can be approximated by its discretized form

$$V_f(t) \approx \sum_{t_{\text{onset}}}^{t_i} \frac{\pi}{6} d_f^3 \Big|_{t_d = \frac{t_{i-1} + t_i}{2}} (\Delta N_f), \quad \text{with} \quad (3)$$

$$\Delta N_f = N_f|_{t_i} - N_f|_{t_{i-1}},$$

where the subscript i represents the index for the sampling point in time, and $d_f(t_d)$ is the diameter of the fragments

shed at t_d . Equation (3) requires as input the fragment number N_f at each time delay, and the instantaneous diameter of the fragments d_f detached at that time. The experimental results on these two parameters will now be discussed. Subsequently, we discuss the length and number of ligaments, and infer their diameters. Relating these quantities allows us to present the instantaneous volume contained in the ligaments V_l .

1. Fragment number

Figure 2(a) presents the fragment number N_f as a function t/τ_c for different combinations of droplet diameter D_0 and pulse energy E_p ; $\tau_c = [\rho D_0^3/(6\sigma)]^{1/2}$ is the capillary time. Each data point represents the mean value of the fragment number obtained from several images (typically 20 images) recorded at the same time delay. For each image, the fragment number is obtained by our fragment-detection algorithm with an auxiliary correction from manual inspections. The performance of this postprocessing is illustrated in the inset of Fig. 2(a). It is shown that our algorithm could fail to correctly identify a fragment when it is (i) too close to its neighbor fragment, (ii) still in a ligament breakup process, and (iii) too far out of focus. These errors are corrected by our manual check. Our data in Fig. 2(a) shows that for a fixed D_0 , a higher pulse energy results in a higher fragmentation rate \dot{N}_f , and also an earlier onset of fragmentation t_{onset} , leading to a larger N_f at a given t/τ_c .

Figure 2(b) presents t_{onset}/τ_c as a function of the deformation Weber number (referred to as the Weber number hereafter) $We_d = \rho \dot{R}_0^2 D_0 / \sigma$ where \dot{R}_0 is the initial expansion speed of the droplet; \dot{R}_0 is determined by a linear fit of the R_r data (following Klein *et al.* [28]) using the first three time frames after the onset of the impact, typically up to 300 ns to 1 μ s. In Ref. [8] the deformation Weber number We_d was first introduced to capture the dynamics of the sheet expansion upon laser impact to a better accuracy than the Weber number based on droplet-propulsion speed [8,9]. Indeed, as motivated in Ref. [8], it is the radial expansion speed of the droplet and not its impact speed that sets the deformation dynamics, and the ratio of these two speeds strongly depends on the impact conditions [14,30]. A similar result was found, in fact, in droplet-pillar impact experiments [37]. Our data indicate an earlier onset of fragmentation with an increasing Weber number. This observation has also been reported for the case of droplet impact on a pillar in Ref. [37], in which a scaling law $t_{\text{onset}}/\tau_c \sim We_d^{-1}$ was found. A fit of this power law to our data is plotted in Fig. 2(b) in a solid line. The prefactor from the fit is 263(23), with the number in the bracket representing the standard error of the fit. This number is in reasonable agreement with the prefactor approximately equal to 320 analytically obtained in Ref. [37].

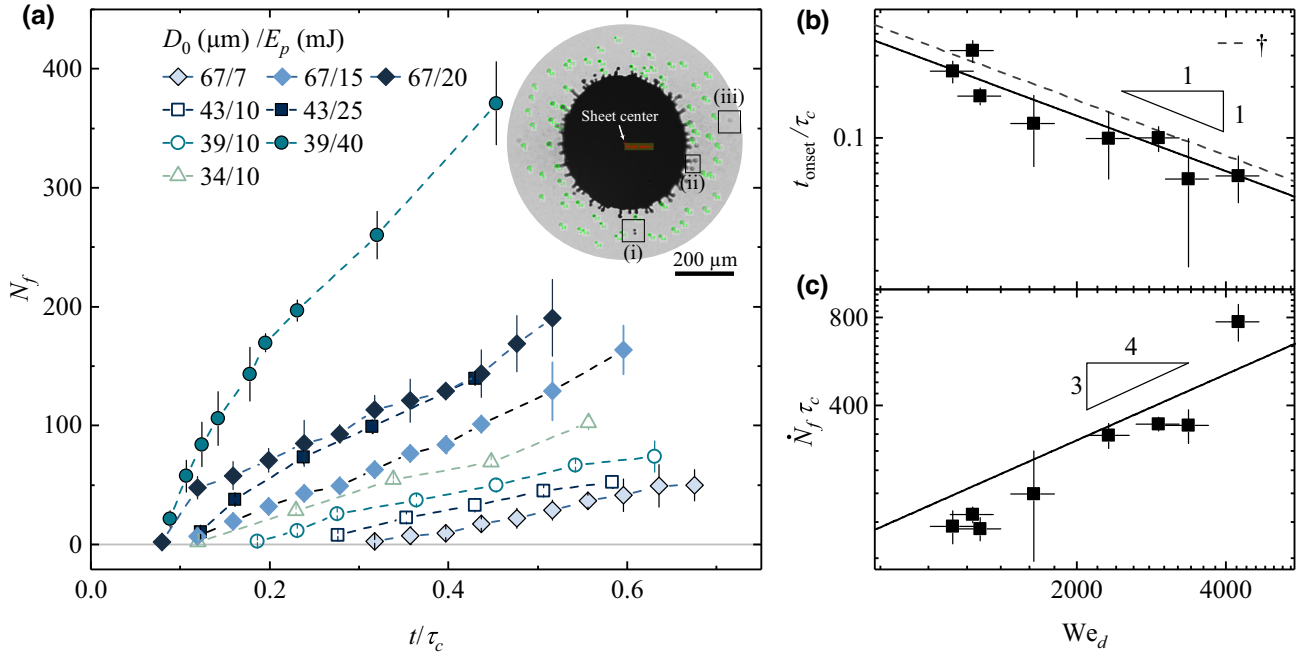


FIG. 2. (a) Fragment number N_f as a function of nondimensional time t/τ_c for different combinations of droplet diameters D_0 and laser pulse energies E_p . The inset shows a front-view shadowgraphy image of an expanding sheet (horizontally stretched to correct for the 30° observation angle) that illustrates the performance of our postprocessing for obtaining the fragment number. Three scenarios where our processing will likely fail to detect fragments are indicated by three boxes (i)–(iii); see the main text. (b) Scaled onset time of fragmentation t_{onset}/τ_c as a function of the Weber number We_d . The solid line is a power-law fit of $t_{\text{onset}}/\tau_c \sim We_d^{-1}$ to the data, which yields a prefactor of 263(23) with the number in the bracket indicating the standard deviation. The dashed line represents $t_{\text{onset}}/\tau_c = 320 We_d^{-1}$ from Ref. [37] (\dagger). (c) Scaled shedding rate $\dot{N}_f \tau_c$ as a function of We_d . The solid line represents the power-law fit of $\dot{N}_f \tau_c \sim We_d^{3/4}$ to the data as proposed in Ref. [16]. The fit yields a prefactor of 1.0(1). A linear-linear representation of the power-law fits and data is provided in the Appendix.

We observe that for most of the time during the shedding process, the increase in fragment number follows a linear trend, hence there is a constant shedding rate \dot{N}_f that depends only on the Weber number. Figure 2(c) presents $\dot{N}_f \tau_c$ as a function of We_d , where \dot{N}_f is obtained by a linear fit to the time domain of N_f where a constant shedding rate is evident. Our graph shows an increase in \dot{N}_f with increasing We_d . In Ref. [16], the fragments are generated with a continuously decreasing rate \dot{N}_f , in contrast with our results in Fig. 2(b). It is yet unclear what is the origin of this difference between our results and those of Ref. [16]. We do note that we also found a disagreement with the same work on the topic of fragment speed in our previous study in Ref. [9]. Therefore, we speculate that both discrepancies have the same root cause and that a detailed study of the ligament growth and fragment pinch-off dynamics is called for. In Ref. [16] a scaling law of $\dot{N}_f \tau_c \sim We_d^{3/4}$ is analytically identified. This scaling is also plotted in Fig. 2(c) and is shown to be in good agreement with our data, where a prefactor of 1.0(1) is used as obtained from a fit to our data.

2. Fragment diameter

Typical fragment diameters studied in this work are at or below the resolution of our imaging system (approximately $3 \mu\text{m}$). To still quantify these diameters under such challenging conditions, we apply machine learning based on a convolutional neural network (CNN). The CNN training data set is obtained from a custom calibration target. This calibration target consists of a series of optically opaque, 200-nanometer-thick gold disks fabricated on a silica substrate with stepped diameters ranging from 1.4 to $10 \mu\text{m}$. The calibration target is imaged using the exact same imaging setup and configuration as used to record the images of the tin target fragments of interest. By recording an image of the calibration target at several focal positions, the training data set is assembled. By including such out-of-focus images, the network is able to correctly identify the size of fragments, even when they are positioned slightly out of focus. More information on the machine-learning method, including the CNN structure, the preprocessing steps applied to each image, and the validation studies performed can be found in the Appendix.

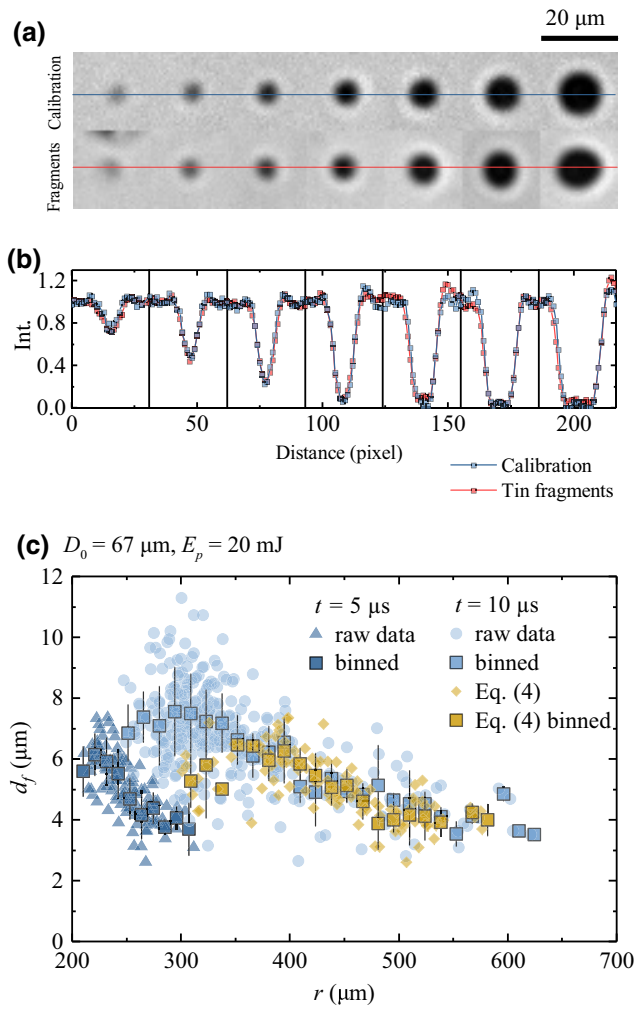


FIG. 3. Fragment diameter d_f determined by machine learning combined with training data obtained from a custom calibration target. (a) First row: example images of the gold disks on our calibration target (used for the training of the network). Second row: images of tin fragments. (b) The horizontal lineout profiles going through the center of first-row images (calibration target, blue) and the center of the second-row images (tin fragments, red) of panel (a). (c) Fragment diameter d_f as a function of radial distance to the center of the sheet r . Results and their corresponding binned data for both $t = 5$ and 10 μs are plotted, where $t = 0$ marks the onset of the laser pulse. Results for $\tilde{d}_f(r)$ at $t = 10$ μs, based on Eq. (4), are also shown.

Figure 3(a) presents images of the gold disks on the calibration target captured by our imaging system at the focal plane (top row), and selected fragments detected in our experiments (bottom row). The images of the tin fragments are, visually, indistinguishable from those of gold disks, indicating that the machine-learning method can accurately determine the size of the fragments within the size range of the calibration targets. The results obtained with the machine-learning method are further supported by

Fig. 3(b), which presents a horizontal lineout for each individual calibration object and fragment shown in Fig. 3(a). To obtain the final fragment-size data, we constrain the eccentricity of the identified fragments. This filter enables us to separate the individual fragments—located within a finite distance from the focal plane (approximately ± 30 μm)—from aggregated fragments or any ligaments that were mistakenly identified as fragments.

Figure 3(c) presents the fragment diameter d_f , as determined with our machine-learning analysis, as a function of the radial distance to the center of the sheet r . The data is obtained for the case where $D_0 = 67$ μm and $E_p = 20$ mJ. The radial distribution of d_f at two different time delays ($t = 5$ μs and $t = 10$ μs) are plotted. Our results show that more outward-located fragments have (i) smaller sizes and (ii) travel faster (as indicated by a longer traveling distance in the r direction). These observations are consistent with the conclusions presented in Ref. [9] on fragment speeds and, as we discuss below, with previous work on droplet-pillar impact [16,33,38]. Since detached fragments travel at constant speeds, the radial distribution of fragment diameters at $t = 10$ μs can be obtained by propagating the distribution $d_f(r)$ at an earlier moment $t = 5$ μs following

$$\tilde{d}_f(r)|_{t=10\ \mu\text{s}} = d_f(r - u_f(r) \Delta t)|_{t=5\ \mu\text{s}}. \quad (4)$$

This radial distribution $\tilde{d}_f(r)|_{t=10\ \mu\text{s}}$ is also plotted in Fig. 3(c) in which the fragment speed u_f at $t = 5$ μs is obtained by our double-frame camera, in line with the steps established in Ref. [9]. It is shown that $\tilde{d}_f(r)|_{t=10\ \mu\text{s}}$ as predicted by Eq. (4) agrees well with the data from direct measurements at $t = 10$ μs. This agreement shows our ability to connect each individual fragment with its diameter d_f and speed u_f that define the trajectory of the fragments. Next, by finding the intersection of the ballistic trajectories of fragments with the radial expansion of the ligament, we acquire the detachment time t_d of each corresponding fragment.

Figure 4 presents d_f as a function of t_d/τ_c . Our observations are consistent with the studies by Wang *et al.* [16,33,38] on a water droplet impacting a pillar. In these studies, the relation between the diameter of the bounding rim, ligaments, and fragments has been studied in detail. First, by invoking momentum conservation on an extrusion of a ligament growing from a continuously decelerating rim, Wang *et al.* [33] found a universal criterion that governs the instantaneous thickness of the bounding rim b_r

$$\text{Bo} = \rho b_r^2 (-\ddot{R}_r)/\sigma = 1, \quad (5)$$

where Bo is the local Bond number of the rim based on its radial deceleration \ddot{R}_r . During the expansion of the sheet, the deceleration scales as $-\ddot{R}_r \sim R_{\text{max}}/\tau_c^2 \sim$

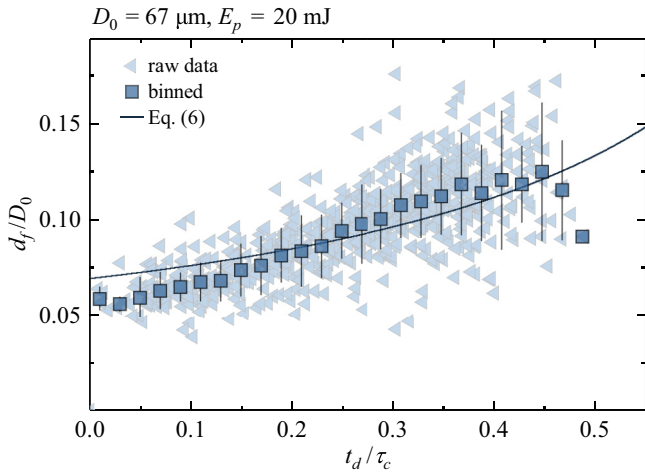


FIG. 4. Scaled fragment diameter d_f/D_0 as a function of its detachment at t_d/τ_c . The solid line presents the prediction from Eqs. (5) and (6). The error bars represent the standard deviation of the binned data.

$(\sigma/\rho R_0^2)We_d^{1/2}$ with $R_{\max} \sim R_0 We_d^{1/2}$ [8]. Substituting this relation into Eq. (5) yields $b_r \sim R_0 We_d^{-1/4}$, consistent with the previous study by Villermaux *et al.* [15]. Next, the relation between the diameters of ligaments w_l and fragments d_f was experimentally investigated in Ref. [16,38] to yield

$$d_f(t) \approx 1.5w_l(t), \quad \text{with} \quad (6)$$

$$w_l(t) = \alpha(t)b_r,$$

where $\alpha(t) = 0.32(t/\tau_c)^2 + 0.24(t/\tau_c) + 0.92$ is a function of t/τ_c solely and varies from 1 to 1.2 during the expansion of the sheet [16]. Values of $d_f(t_d)$ predicted by Eqs. (5) and (6) are depicted in Fig. 4 by a solid line. The deceleration of the sheet \ddot{R}_r as input for the relation $Bo = 1$ is obtained by fitting a third-order polynomial to the expansion trajectory of the rim R_r for the corresponding data set. Figure 4 presents good agreement between the analytical prediction and our results. This agreement may be seen to either verify our determination of fragment diameter or, alternatively, to demonstrate the robustness of Eq. (6). Given the agreement shown in Fig. 4, we decide to employ Eq. (6) for the discussion below on the global volume fractions.

3. Ligament length

Next, we determine the instantaneous volume contained in the ligaments V_l . A single ligament can be described as a cylinder with a length L_l and a diameter w_l , hence a volume $\pi w_l^2 L_l/4$. We first discuss the experimental results for the ligament length. The length of each ligament is determined by the radial distance from the tip of the ligament to the rim. The detection of the rim and the tip of the ligament follows the method detailed in Ref. [9]. The values of ligament diameter w_l are extracted from Eq. (6).

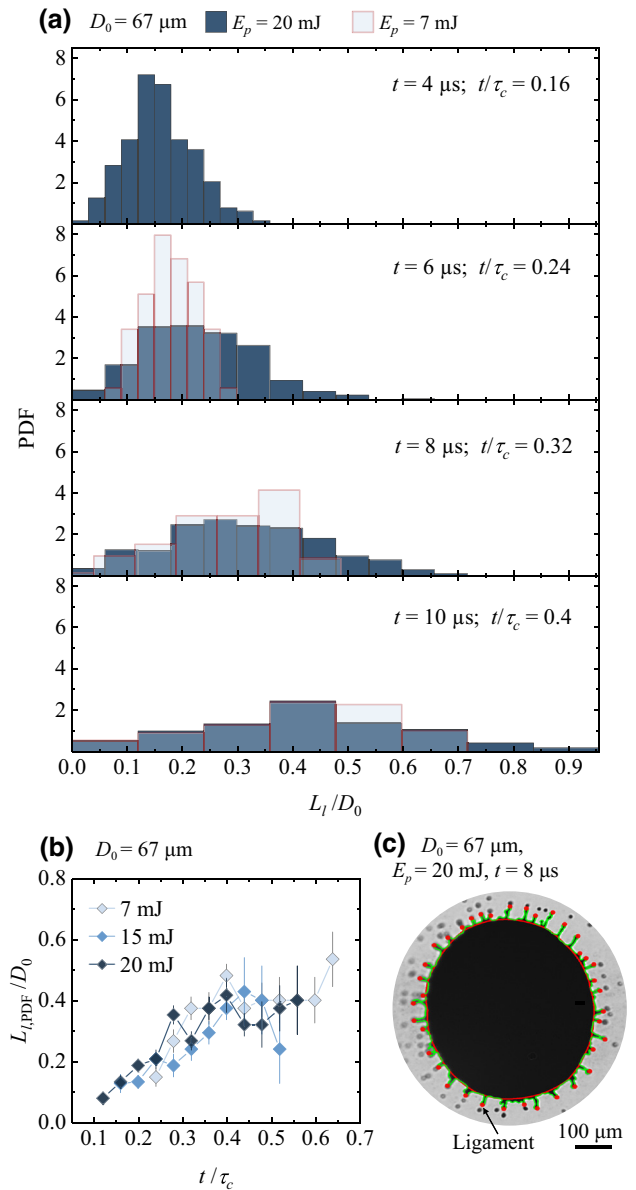


FIG. 5. (a) Probability density function (PDF) of scaled ligament length L_l/D_0 for four different time delays, obtained with $D_0 = 67 \mu\text{m}$ and $E_p = 7$ and 20 mJ. Ligaments did not significantly develop beyond mere corrugations at $t = 4 \mu\text{s}$ for the $E_p = 7$ mJ case, and subsequently no corresponding PDF is shown. (b) The most probable length of ligament $L_{l,\text{PDF}}$ as a function of nondimensional time t/τ_c for three different pulse energies (see legend). The error bar shown equals the bin width in panel (a). (c) A front-view shadowgraphy image of a sheet (horizontally stretched to correct for the 30° observation angle) to illustrate the outer contour (green) and the inner contour (red). The image is captured at $t = 8 \mu\text{s}$ with $D_0 = 67 \mu\text{m}$ and $E_p = 20$ mJ. Each ligament tip, which is detected from the outer contour is indicated by red dots.

Figure 5(a) presents the probability density function (PDF) of the ligament length scaled by the initial droplet diameter L_l/D_0 ($D_0 = 67 \mu\text{m}$) at four different time delays

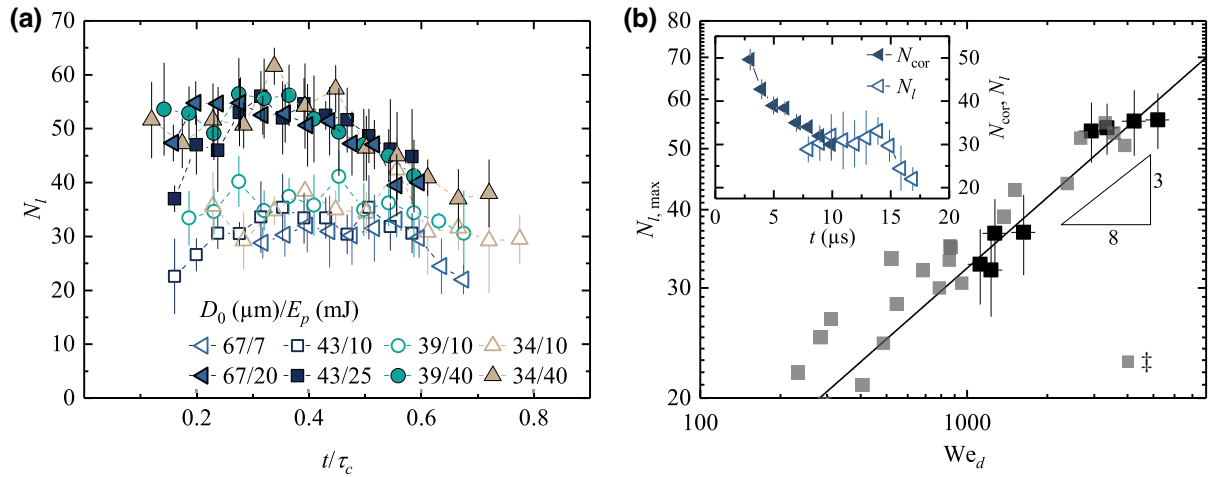


FIG. 6. (a) Ligament number N_l as a function of t/τ_c for different combinations of droplet diameters D_0 and the pulse energies E_p (see the legend). (b) $N_{l,\max}$ obtained as the average ligament number surrounding its apex value as a function of the Weber number We_d . Data from Ref. [8] (\dagger) are reproduced in the graph. The solid line represents a power-law fit of $N_{l,\max} \sim We_d^{3/8}$ to the results of our study, which yields a prefactor of 2.4(1) with the number in the bracket representing the standard deviation from the fit. A linear-linear representation of the power-law fit and data is provided in the Appendix. The inset shows corrugation number N_{cor} and the ligament number N_l as a function of t for the data set of $D_0 = 67 \mu\text{m}$ and $E_p = 7 \text{ mJ}$.

after laser-pulse impact. The results of two pulse energies are presented ($E_p = 7$ and 20 mJ). Our results show that for both pulse energies the ligament length increases with time, with an increasing most-probable-length $L_{l,\text{PDF}}$. The spreading of L_l (i.e., the PDF width) increases with time as old ligaments grow, while new ones are generated. For low energies (low We numbers) this spreading width is smaller, in particular at early times, given that fewer ligaments grow and fragment at a lower rate (see Secs. III A 1 and III A 4). The increase in $L_{l,\text{PDF}}$ over time is shown in Fig. 5(b) in which $L_{l,\text{PDF}}$ for three different pulse energies are presented, that is, $E_p = 7, 15,$ and 20 mJ , with the corresponding deformation Weber number $We_d = 1200, 2300,$ and 3300 , respectively. Figure 5(b) also shows that the growth of $L_{l,\text{PDF}}$ is rather independent of the pulse energy (also see Sec. III A 5). It should be noted that an accurate estimate of L_l by our postprocessing requires that the ligaments protrude radially from the rim. Any deviation from an outward-oriented cylindrical shape will lead to an underestimate of the actual length of the ligament. Any such angular deviations are typically well below 10° leading to a systematic error of just 2% (in few, extreme and late-time cases, angles of up to 30° are observed, leading to a still modest underestimation of 13%).

4. Ligament number

In addition to ligament length, the postprocessing illustrated in Fig. 5(c) yields ligament number N_l for each processed image. Figure 6(a) presents N_l as a function of t/τ_c for different combinations of droplet diameter D_0 and pulse energy E_p . It is shown that for a given droplet size,

a larger number of ligaments is induced by a higher pulse energy. Furthermore, once the first ligaments are detected by our postprocessing, we observe a slight increase in their number over time, reaching a maximum at $t \approx 0.3 - 0.5 \tau_c$. Later, N_l decreases, mainly due to the merging of ligaments [8,9,38].

Figure 6(b) presents $N_{l,\max}$ as a function of We_d . The value of $N_{l,\max}$ for each data set is obtained by averaging the ligament number ranging from two frames in time preceding the maximum of N_l to two frames after that moment. A power-law fit of $N_l \sim We_d^{3/8}$ is performed to the data and yields a prefactor of 2.4(1). This power law has been analytically proposed in Ref. [8] where it has been further confirmed experimentally for the case of laser impact on a droplet with $D_0 = 50 \mu\text{m}$. These data are reproduced in Fig. 6(b), showing their agreement with the results of our measurements.

The scaling $N_l \sim We_d^{3/8}$ has also been reported by Wang *et al.* [16] for the case of pillar impact. We note, following Ref. [16], that measurements of the number of ligaments should be distinguished from those of initial corrugations—the early time manifestation of capillary instabilities arising on the rim. Only a fraction of the corrugations develop into ligaments. This phenomenon is also observed in our case (cf. Ref. [9]) where both the temporal and spatial dimensions are drastically smaller than those in Ref. [16]. The inset in Fig. 6(b) shows the number of corrugations N_{cor} and ligaments N_l for the case with $D_0 = 67 \mu\text{m}$ and $E_p = 7 \text{ mJ}$. We note that N_{cor} is determined through a direct visual inspection. It is clearly shown that the corrugation number decreases, with only part of them becoming ligaments at later moments.

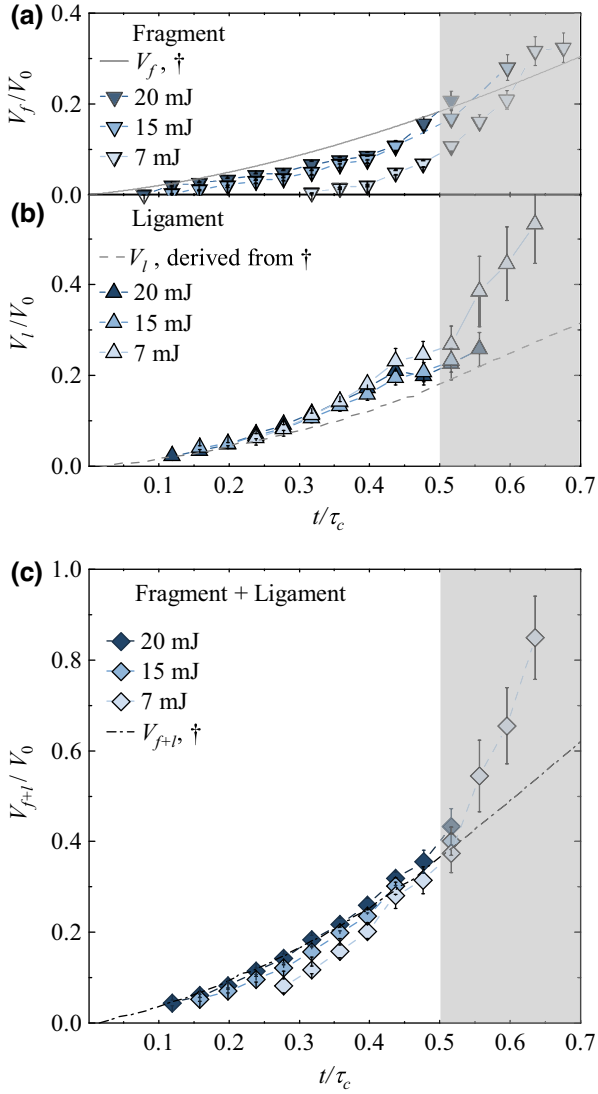


FIG. 7. (a),(b) Volume ratio of the fragments V_f and ligaments V_l with respect to that of the initial droplet V_0 as a function of t/τ_c . The droplets have initial diameters of $D_0 = 67 \mu\text{m}$. (c) The sum of fragment and ligament volume $V_{f+l} = V_f + V_l$ with its ratio to V_0 as a function of t/τ_c . The solid and dash-dotted lines presented in (a),(c), respectively, plot the predictions on V_f/V_0 and V_{f+l}/V_0 from Ref. [27] (\dagger). From that study, the volume of ligaments is derived as $V_l = V_{f+l} - V_f$ and is plotted as a dashed line in (b). The shaded area indicate the temporal range of $t > 0.5\tau_c$.

5. Results of fragment and ligament volume

With the measurements of the key parameters at hand, we are now in the position to determine the volume taken up by fragments and ligaments. Figure 7(a) shows the volume ratio V_f/V_0 as a function of t/τ_c . Each V_f data point is determined following Eq. (3) with N_f retrieved from the experimental data shown in Fig. 2, and $d_f(t_d)$ obtained from Eq. (6). The application of Eq. (6) is supported by the agreement between the model and our machine-learning

results on $d_f(t_d)$ presented Fig. 4. Given the temporal range of the comparison in Fig. 4 (i.e., $t \lesssim 0.45\tau_c$) and also the validity range $t \lesssim 0.5\tau_c$ for $\text{Bo} = 1$ for which the rim requires a sufficiently large deceleration [6,33], we apply Eq. (6) to the determination of d_f and V_f up to $t = 0.5\tau_c$. Figure 7(a) presents a continuous increase in V_f over time: a progressive detachment of liquid into fragments. Furthermore, the results for the $E_p = 15$ and 20 mJ cases are almost indistinguishable although the $E_p = 20$ mJ case presents nearly twice the amount of fragments compared to the $E_p = 15$ -mJ case at any given time cf. Fig. 2, with the higher-impact energy case producing smaller fragments. For the case of $E_p = 7$ mJ, less liquid is channeled into the fragments at early times. This peculiarity is mainly due to the strongly delayed fragmentation onset moment for the small energy case: $t_{\text{onset}}/\tau_c \approx 0.3$ for $E_p = 7$ mJ, as compared to $t_{\text{onset}}/\tau_c \approx 0.1$ and 0.06 for $E_p = 15$ and 20 mJ, respectively [cf. Fig. 2(b)]. Figure 7(b) presents the volume ratio of the ligaments to the initial droplet V_l/V_0 as a function of t/τ_c . In addition to the observation of a continuous increase in V_l over time, our results indicate that there is no evident dependence of V_l on the pulse energy and, thus, on the Weber number. The independence of V_f/V_0 on the Weber number is expected when substituting the power laws $\dot{N}_f \tau_c \sim \text{We}_d^{3/4}$ [cf. Fig. 2(c)] and $d_f \sim D_0 \text{We}_d^{-1/4}$ (cf. Sec. III A 2) into Eq. (2), yielding $V_f/V_0(t/\tau_c)$ that is determined by t/τ_c solely, consistent with Wang *et al.* [27]. The volume of ligaments scales as $V_l \sim w_l^2 N_l L_l \sim D_0^3 \text{We}_d^{-1/8} L_l$ following $w_l \sim D_0 \text{We}_d^{-1/4}$ and $N_l \sim \text{We}_d^{3/8}$ [cf. Fig. 6(b)]. The scaling of V_l would indeed be independent of the Weber number if here the relevant ligament length scales as $L_l \sim \text{We}_d^{1/8}$, which is consistent with the scaling of the necking time approximately $\text{We}_d^{-3/8}$ and radial flow speed approximately $\text{We}_d^{1/2}$, which together would set a typical length scaling as $\sim \text{We}_d^{1/8}$. For the data shown in Fig. 7(b), the Weber number ranges from 1200 to 3300, thus giving a very limited, and indeed unobservable predicted change of approximately 10% on L_l [cf. Fig. 5(b)] given the postulated weak dependence on the Weber number $\text{We}_d^{-1/8}$. More data, taken over a wider range of Weber numbers, would be required to experimentally verify the scaling of the ligament length.

The temporal evolution of V_f and V_l has been studied previously by Wang *et al.* [27] for water droplet impact on a pillar. In that work, the sum of ligament and fragment volume represents the liquid shed from the rim $V_{f+l} = V_l + V_f$. The ratio V_{f+l}/V_0 , and the ratio V_f/V_0 contributing to it were separately shown to be functions of t/τ_c only and are independent of the droplet's Weber number. As a corollary, V_l/V_0 should also be a function of t/τ_c only, independent of the Weber number. Figures 7(a) and 7(b) show reasonable agreement between our experimental results and the predictions from Ref. [27]. The slightly lower volume channeled into the fragments, comparing to

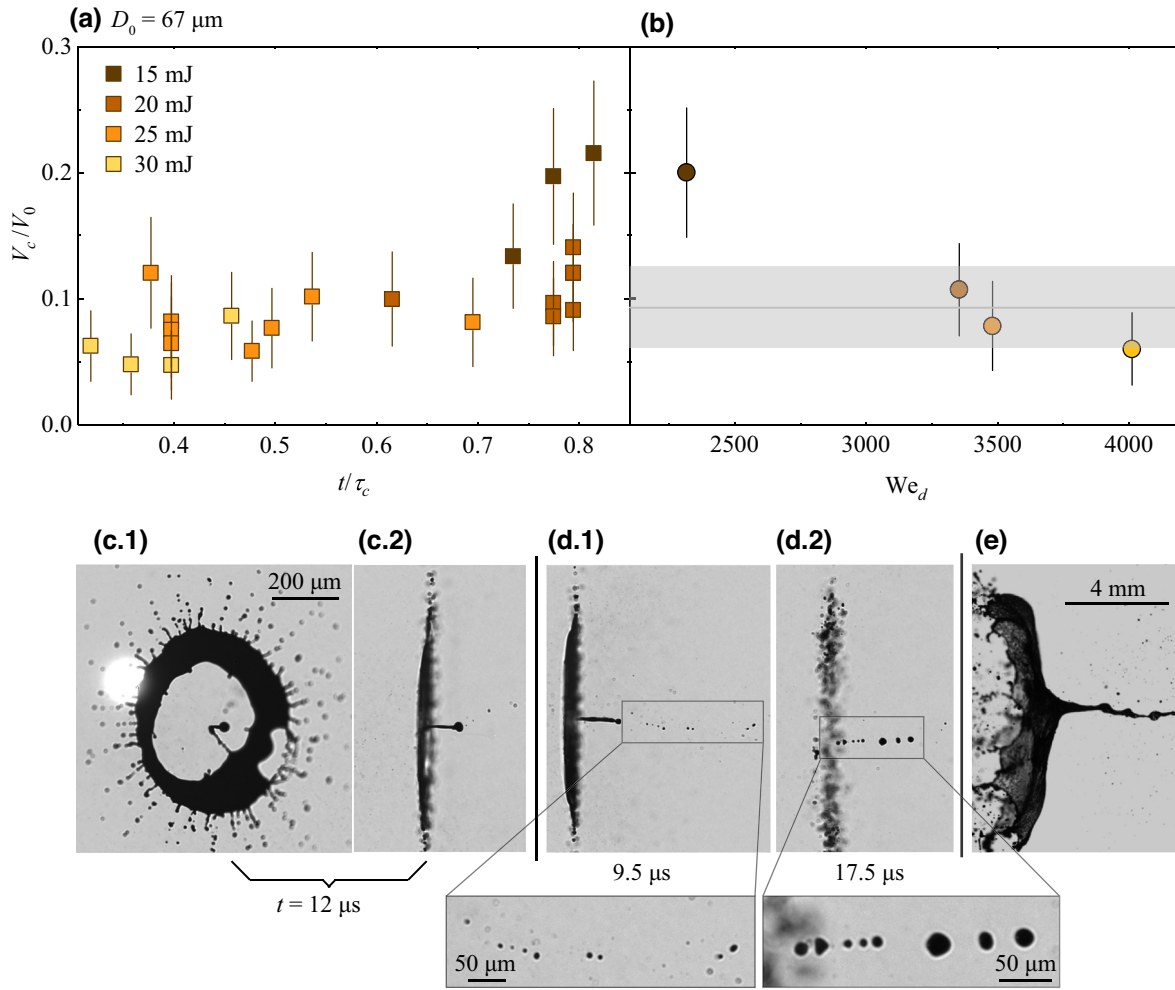


FIG. 8. Volume ratio of the center mass to the initial droplet V_c/V_0 as a function of (a) t/τ_c , and (b) the Weber number We_d . Droplets have initial diameters of $D_0 = 67 \mu\text{m}$. In panel (b), the horizontal line at $V_c/V_0 = 9(3)\%$ presents the average of the four data points; the number in the bracket gives the standard deviation, indicated by the shaded area around the horizontal line. (c.1),(c.2) Front and side view of a sheet with its center mass and the associated center jet visible. (d.1),(d.2) Side-view images showing two examples of the center mass that reforms into a continuous stream [(d.1)] or a series of droplets [(d.2)]. The enlarged inset of (d.1) shows some fine droplets, which detach from the jet at early times. (e) A side view of a MEK liquid droplet impact by a laser pulse, taken and adapted from Ref. [8]. Note the change in length scale.

the model predictions, is shown to be offset by a modestly larger volume channeled into the ligaments—to yield a near-perfect agreement between model and experiment for V_{f+t}/V_0 in the applicable time domain, as shown in Fig. 7(c).

B. Volume of the center mass

During the expansion of the droplet, a disk-shaped feature may appear in the center of the sheet [6,7]. The formation of such a center mass is hypothesized to originate from early-time laser-induced cavitation and cavity collapse inside the droplet [8,35]. In some cases, laser impact may lead to jetting. Such jetting has also been observed by Klein *et al.* [8] for laser impact upon a liquid methyl-ethyl-ketone (MEK) droplet [see Fig. 8(e)].

In our previous work in Ref. [6], we identified this center mass as a separate channel in the liquid distribution in the target and excluded its volume from that of the sheet V_s . The thickness of the center-mass disk could not be directly assessed due to experimental limitations. However, our initial observations did indicate that the center disk is significantly thicker than the surrounding sheet, and its contribution to the overall mass balance should thus be taken into account. During the sheet expansion, the center mass is bounded by a much thinner halo [6]. Meanwhile, spontaneously formed holes will appear on the sheet when the amplitude of capillary instabilities exceeds the thickness of the sheet [8]. These holes could open in the bounding halo of the center mass. Once the holes appear, the edges of these holes expand with the Taylor-Culick speed, which increases with decreasing local thickness.

Therefore, the relatively thin halo around the center mass retreats promptly, separating the center mass from the rest of the sheet. This phenomenon ceases the exchange of liquid between the center mass and the sheet, effectively maintaining the amount of liquid of the center mass during the rest of the expansion. Figure 8(c.1) presents a front view of a sheet to exemplify the separation of the center mass from the rest of the liquid. The corresponding side-view image is shown in Fig. 8(c.2). As time passes, the detached center mass collapses as a result of the surface tension, forming either a spherical droplet or a center jet that can be described by the shape of a cylinder [see panels (c.2) and (d.1)]. The jet could further break into a series of small droplets due to a Rayleigh-Plateau instability, as shown in Fig. 8(d.2) with its inset showing an enlargement on these droplets. We determine V_c from the volume of these associated geometries (i.e., the cylindrical liquid jet or spherical droplets) from our 90° side-view images with their improved resolution compared to our previous studies, and using the largest, $67\text{-}\mu\text{m}$ droplet size for optimum visibility.

Figures 8(a) and 8(b) show the volume ratio of the center mass to the initial droplet V_c/V_0 as a function of t/τ_c , and the Weber number We_d , respectively. Our results in Fig. 8(a) indicate that a 5–20% fraction of V_0 is channeled to the center mass, with the precise number depending on the experimental parameters. There is no evident dependence of V_c/V_0 on time. Figure 8(b) shows that a larger pulse energy appears to reduce the fraction of tin in V_c . Further studies are required to fully quantify and to clarify the origin of the center-mass feature. In particular, the influence of the initial droplet size needs to be addressed in future work: the droplet size dictates the acoustic timescale [34] and the deposited laser energy per droplet volume (cf. Ref [39]), which in turn characterize the degree of compressibility of the flow and could influence the formation of the center mass.

Averaging the available data in Fig. 8(b) yields a fraction of 9(3)% for the center mass, which we use in the following discussion for the global volume distribution. We note that the obtained volume of the center mass may be slightly smaller than the actual volume as some of the liquid shed from the center jet may appear in the form of fine particles, see the enlarged inset of Fig. 8(d.1). These particles detach at an early time from the center of the sheet and travel forward at high speeds. Therefore, they quickly move out of the field of view of our side-view images and thus cannot be captured by our measurements.

C. Volume of ablated material

When a tin microdroplet is irradiated with a laser pulse, a fraction of liquid material at the surface of the droplet is transformed into plasma that expands away from the droplet. This expansion provides a momentum kick to

the droplet, which results in a radial expansion and a propulsion velocity of the droplet along the laser direction [8,14,29,30,40]. The volume of ablated material V_a can be obtained from the data underlying our numerical study in Ref. [30], where detailed radiation-hydrodynamic simulations by RALEF-2D were performed to examine the partitioning of kinetic energy between propulsion and expansion. Based on simulations for two different droplet sizes $D_0 = 27$ and $45\ \mu\text{m}$, impacted by laser pulses with energy E_p ranging in $0.5\text{--}30\ \text{mJ}$ and $20\text{--}104\ \mu\text{m}$ (FWHM) beam size, the ablated material accounts for 5–23% of the initial amount of tin. With these numerical settings, the droplet is conditioned with a propulsion and expansion speed ranging from 30 to 250 m/s, yielding a wide range of Weber number from 600 to 15 000. The scaling of V_a/V_0 with We_d and D_0 is highly nontrivial given the complex interplay of the underlying physical processes. The simulations show a monotonic increase of V_a/V_0 with increasing We_d and a decrease with increasing D_0 . A fit to the simulation data results in an approximate, heuristic scaling relation of the ablated fraction $\sim D_0^{-\beta} We_d^\gamma$, with $0.6 \leq \beta \leq 0.8$ and $0.3 \leq \gamma \leq 0.5$. This scaling relation is only applicable for a limited parameter range and does not capture the full set of dependencies. For one of the cases studied, our simulations indicate that approximately 16% of the total material will be ablated when a droplet with a diameter of $27\ \mu\text{m}$ is impacted by a laser pulse with energy of 4 mJ and beam diameter of $50\ \mu\text{m}$ (FWHM). As a result, the droplet is accelerated to a speed of 144 m/s along the laser direction. Propelling the droplet with the same size instead to 219 m/s would require a laser pulse energy of 8 mJ, ablating 23% of the initial mass, consistent with the approximate scaling relation.

D. Volume of the sheet

In this section, we recapitulate our previous experimental measurements on the volume of the sheet [6,7]. Given that the droplet expands into an axisymmetric sheet, the volume of the sheet can be determined by spatial integration of the thickness profile. These thickness profiles—for a wide range of pulse energies and three different droplet sizes—were experimentally measured in Refs. [6,7] by (i) determining the opening velocity (Taylor-Culick speed) of spontaneously formed holes on the sheet, and (ii) the partial transmissivity of the backlight through the sheet, and (iii) by using a probe pulse that gradually removes the liquid from the sheet. Our results revealed that a sheet with a thickness of several tens of nanometers is formed a few microseconds after the laser impact. The thickness profile $h(r)$ presents a slender spatial gradient, where h decreases with radial distance to the center of the sheet r . With further spatial integration, we provided the volume of the sheet V_s in a time range of $t/\tau_c \in (0.15, 0.7)$. The data of V_s indicates a continuous loss of tin from the sheet. Furthermore,

we showed that the volume ratio V_s/V_0 depends on the nondimensional time t/τ_c only and is independent of the Weber number.

This self-similar curve for the thickness in combination with the sheet expansion trajectory produces a description of the time evolution of the sheet volume V_s . We note that at early times, the slender-slope approximation [15,23–25], underpinning the self-similarity, no longer applies to the sheet. As a result, we cannot expect that our self-similar curve for the thickness profile and the corresponding description for the sheet volume are valid for early-time dynamics.

E. Volume of the rim

The bounding rim can be described by the shape of a curved cylinder with a length of $2\pi R_r$ and a diameter of b_r . Therefore, its volume reads $V_r = (\pi^2/2)R_r b_r^2$. The length of the rim $2\pi R_r$ has been well captured by our experiments with the postprocessing that determines the radial position of the rim [see Fig. 5(c)]. However, direct measurements of the thickness of the rim b_r are still lacking. Our experiments elaborated in Ref. [7] confirmed the presence of the rim, where it is directly visualized with a vaporization pulse—a pulse designed to remove the fluid from the thin sheet [see Fig. 1(c)]. Regardless, the yet unknown mass fraction removed from the rim by this vaporization pulse prevents an accurate determination of b_r . Moreover, the subresolution size of b_r would make an estimation of its volume through direct optical inspection particularly challenging.

To still determine the volume of the rim, we employ the robust relation for the local Bond number $\text{Bo} = \rho b_r^2 (-\dot{R}_r)/\sigma = 1$ [i.e., Eq. (5)] that universally governs the instantaneous thickness of the rim [33]. The relation $\text{Bo} = 1$ is valid for inviscid flow, which is applicable in our case where the Reynolds number $\text{Re} = D_0 \dot{R}_0/\nu \sim 10^4$ given the viscosity $\nu = 0.26 \times 10^{-6}$ m²/s of liquid tin [41]. As a result, the volume of the rim can be determined as

$$\begin{aligned} \frac{V_r}{V_0} &= \frac{(\pi^2/2)R_r b_r^2}{\pi D_0^3/6} \\ &= \frac{0.26}{0.93 - (\frac{t}{\tau_c})} \left[\left(\frac{t}{\tau_c}\right)^3 - 2.79\left(\frac{t}{\tau_c}\right)^2 + 1.72\left(\frac{t}{\tau_c}\right) + 0.11 \right]. \end{aligned} \quad (7)$$

Equation (7) indicates that V_r/V_0 is a function of t/τ_c only. This is expected as $b_r^2 \sim D_0^2 \text{We}_d^{-1/2}$ and $R_r \sim D_0 \text{We}^{1/2}$, rendering $b_r^2 R_r / D_0^3$ independent of the Weber number.

F. Global mass partitioning

So far, we discuss the volume fraction of liquid taken up by various channels. In our experiments, we systematically alter the Weber number $\text{We}_d = \rho \dot{R}_0^2 D_0 / \sigma$ by varying the

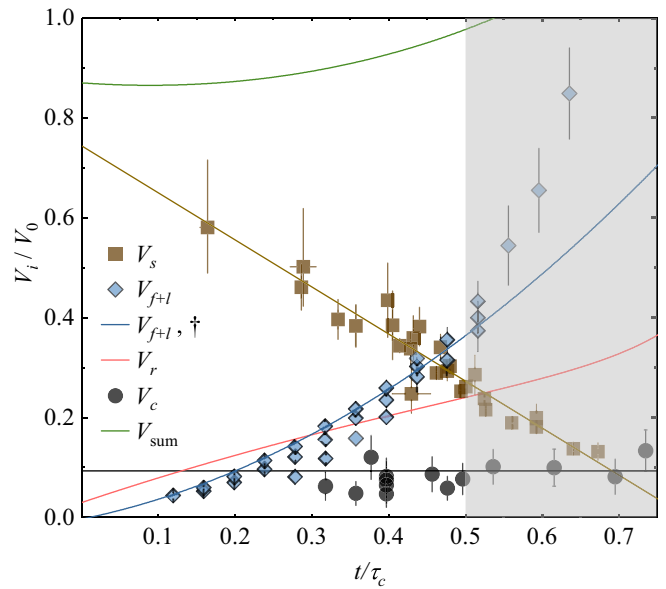


FIG. 9. Volume fraction of different channels with respect to the initial droplet V_0 as a function of t/τ_c . The volume of the sheet V_s is reproduced from the experimental data presented in Refs. [6,7], along with a heuristic linear fit. The summed volume of fragments and ligaments V_{f+l} is from Fig. 7(c), along with the prediction on V_{f+l} from Ref. [27] (\dagger). The red line represents Eq. (7) for the volume of the rim V_r . The volume of the center mass V_c is reproduced from Fig. 8(a), along with a horizontal line at 9% representing the mean values of the data shown in Fig. 8(b). The sum of all these channels $V_{\text{sum}} = V_s + V_{f+l} + V_r + V_c$ is plotted by a green line. The shaded area indicates the temporal range of $t > 0.5\tau_c$ where the assumptions underpinning the models are invalid (see the main text).

droplet diameter D_0 and the pulse energy E_p , which jointly determine the different initial expansion speeds of droplets \dot{R}_0 .

Our observations allow us to summarize the complete liquid distribution in Fig. 9, which presents the volume ratio of all channels (except V_a) listed in Eq. (1) as sole functions of t/τ_c . We exclude the volume of ablated material V_a from the graph given that the material ablation occurs instantly (within 10 ns) after the start of the laser pulse and hence V_a is not a variable changing with t/τ_c throughout the droplet expansion process. The data for V_s from Refs. [6,7] are reproduced in the graph. Furthermore, we sum up the volume of these channels, that is, $V_{\text{sum}} = V_s + V_r + V_c + V_{f+l}$. To plot V_{sum}/V_0 , a heuristic linear fit is performed to the data of V_s/V_0 in order to produce a continuous description of V_s based on experimental data. For a continuous description of V_{f+l} , the model from Ref. [27] is used. This model has been shown to agree with our experimental data [cf. Fig. 7(c)]. For the volume of the center mass, a constant fraction of 9% is added to V_{sum}/V_0 given the fact that there is no evident dependence

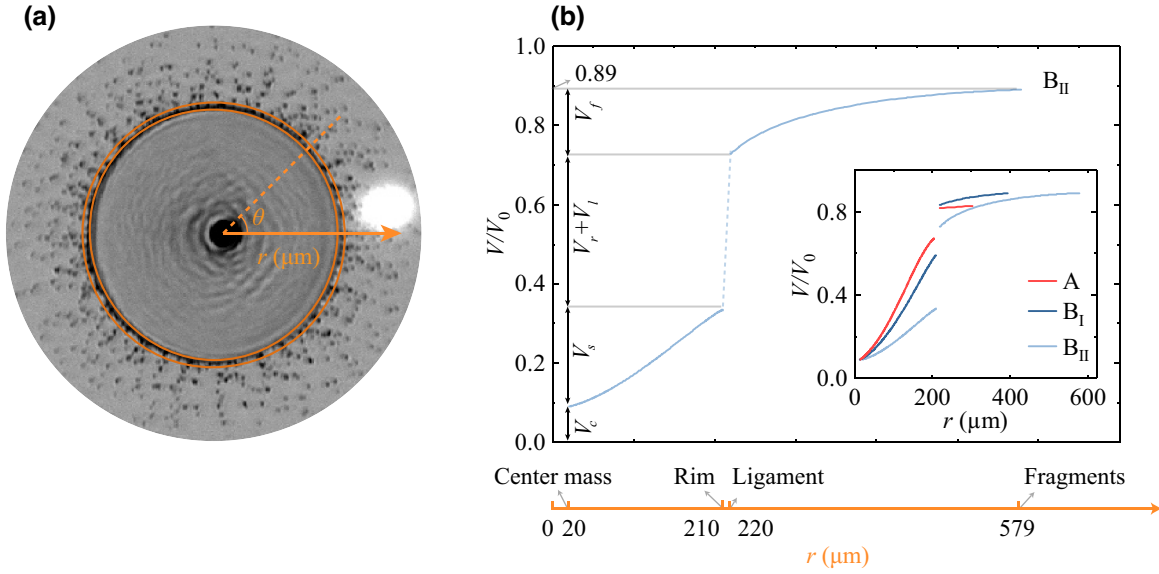


FIG. 10. Spatial distribution of liquid-tin volume. (a) A front-view shadowgraphy image of target B_{II} . The contrast of the image is modified for a better visual on the fine rim, ligaments, and fragments. The image is horizontally stretched to correct for the 30° observation angle. A polar coordinate (r, θ) with its origin at the center of the sheet is depicted. We also draw two concentric circles, with the inner one (with a radius of $210 \mu\text{m}$) representing the location of the rim, and the outer one (with a radius of $210 + 10 \mu\text{m}$) indicating the approximate position of the ligament tip. (b) The cumulative volume fraction of tin as a function of r for target B_{II} , while the results for target A and B_I are included in the inset. The r axis in the polar coordinate [depicted in (a)] is plotted at the bottom, with the radial position of the center-mass edge ($20 \mu\text{m}$), rim ($210 \mu\text{m}$), ligament tip ($220 \mu\text{m}$), and the outermost fragments ($579 \mu\text{m}$). For all three targets, the volume fraction taken up the center mass is set as 9% (cf. Fig. 8). The segment curves representing the sheet volume are determined by integrating the thickness profile $h(r)$ reproduced from Ref. [7]. The volume fractions taken by the rim and ligaments are determined by Eq. (7), and by V_l shown in Fig. 7(b), respectively. Curves that represent fragment volume are obtained by combining the descriptions of fragment speeds provided by Ref. [9] and the data of V_f presented in Fig. 7(a).

of V_c/V_0 on t/τ_c for the fixed droplet size $D_0 = 67 \mu\text{m}$ presented in Fig. 8. The obtained V_{sum}/V_0 is represented by a green curve in Fig. 9. Our results indicate that V_{sum}/V_0 captures approximately 90% of the original droplet volume in the applicable domain. The “missing” volume fraction of approximately 10% to V_{sum}/V_0 is consistent with the expected volume of the ablated material V_a/V_0 , which accounts for 5–23% (cf. Sec. III C). Therefore, we validate Eq. (1) with reasonable accuracy. This observation is remarkable given the complexity of the interplay between the underlying physical processes, and the experimental and theoretical approaches as represented in Fig. 9. We note that V_{sum} becomes larger with increasing time. This observation could be an intrinsic consequence of the systematically higher pulse energies and smaller droplets that correspond to the data of V_s for the early times taken from Refs. [6,7]. Such conditions lead to a larger fraction of ablated material, leading to smaller V_s and, hence, a smaller V_{sum} .

IV. APPLICATION PERSPECTIVE

The volume ratio of all loss channels with respect to the original droplet volume can be characterized by the nondimensional time $t/\tau_c = t/[\rho D_0^3/(6\sigma)]^{1/2}$ solely. In other

words, given a droplet diameter D_0 , time is the key parameter determining the tin volume distribution in a target. As a corollary, to minimize the tin lost from the sheet to the fragments, it is best that the successive laser pulse (e.g., the main pulse) following the prepulse with a minimum time delay (i.e., “shoot early”). To allow the tin target to reach a sufficient size in this short time to provide an optimal geometrical overlap with the large main pulse, an energetic prepulse is needed to induce a higher expansion rate of the droplet (i.e., “shoot hard”). Furthermore, as a direct result of a larger V_s , a larger sheet thickness will be available (i.e., more tin is available for interacting with the main pulse), and scaling to larger main-pulse energies—and more output EUV light—may be feasible in this case.

Figure 10 presents the spatial distribution of liquid-tin volume on three targets, which correspond to targets dubbed A, B_I , and B_{II} as presented in Ref. [7]. Briefly, these targets are obtained by using laser pulses with $E_p = 20 \text{ mJ}$ [target A ($1.2 \mu\text{s}$)] and 12 mJ [target B_I ($2.1 \mu\text{s}$), B_{II} ($3.1 \mu\text{s}$)], respectively, focused down to a spot size of $55 \mu\text{m}$ at the location of the droplet with a diameter $D_0 = 29 \mu\text{m}$. The targets share a common sheet diameter relevant for application—but present very different morphologies. For example, our results show a steep

gradient of the mass distribution at the rim and ligaments: for target B_{II} almost 40 % of the total mass is located within a narrow ring with a width of approximately 10 μm. This “localized mass” could be a source of inefficient usage of the tin by the main pulse or the second prepulse. Furthermore, the *shoot early, shoot hard* solution (target A) will lead to a smaller area over which the liquid debris is dispersed: at equal sheet “target” size, the outer fragments are closer to the rim [7] and cf. Fig. 10.

Another application may be found in the ability to define a predefined spatial shape of the main pulse or other secondary pulses [7], implemented in such a way that it relates to the spatial characteristics of the sheet (see Fig. 10). This approach may lead to a more efficient utilization of the tin material and reduce the required laser energy in the EUV light-generation process. For example, the local fluence of such pulses may be matched to the local thickness of the sheet.

V. CONCLUSION

We present results on the mass partitioning on a liquid-tin target produced by laser-pulse impact on a tin microdroplet. Experimental studies are combined with a pre-existing model from Refs. [16,33] that governs the thickness of the sheet’s rim, significantly extending the range of Weber number over which the robustness of the model is tested. The temporal evolution of the mass fraction in the sheet, the rim, and the summed channel of the fragments and ligaments is demonstrated to be independent of the droplet’s Weber number, and can be described as a sole function of time t/τ_c . The full mass distribution is obtained when also accounting for the mass situated in a center-mass feature and for the mass lost through laser ablation.

Our results of the mass partitioning of fragmenting tin sheets provide a guide toward optimum utilization of the tin mass in EUV sources for nanolithography using a dual-laser recipe (i.e., prepulse—main pulse). We provide recommendations concerning both the delay between the prepulse and successive pulses, and the spatial fluence profile of such pulses. These recommendations aim to minimize any contaminating debris, and to maximize the utilization of tin mass for EUV generation. In addition to the industrial applications, the fundamental insight gained by the comparisons between the cases of laser impact and pillar impact is helpful to expand the scope of applications of the related universal laws.

ACKNOWLEDGMENTS

This work has been carried out at the Advanced Research Center for Nanolithography (ARCNL). ARCNL is a public-private partnership with founding partners UvA, VU, NWO-I and ASML, and associate partner RUG. This project has received funding from European Research

Council (ERC) Starting Grant No. 802648 and is part of the VIDI research program with Project No. 15697, which is financed by the Dutch Research Council (NWO).

APPENDIX

1. Fragment size determination with machine learning

The typical diameter of the tin fragments of interest, those expelled by the expanding sheet as presented in Sec. III A 2, are close to or below the resolution of our imaging system. This, combined with the partial coherence of the back-lighting source, leads to a nontrivial size determination of the fragments. However, every combination of a fragment size and its position in the focal plane will result in a unique image. Therefore, a rigorous physical model, taking into account the specifics of the experiment, would thus still be able to determine the size of such fragments. Such a model would have to include, among others, the point spread function and the precise temporal and spatial coherence properties of our imaging system and illumination, respectively. Instead of developing such a highly complex model we turn to machine learning, and more specifically a CNN, to obtain the fragment diameters d_f . To train the CNN we make use of a custom-manufactured calibration target. This target consists of 200-nm-thick, optically opaque Au disks of various diameters (characterized with an atomic force microscope), fabricated on a silica substrate. All CNN training is performed using the images obtained from these Au disks. We further perform validation studies on two independent data sets. One of Ni particles deposited on a silica substrate and one with free-falling Ag-coated silica spheres. In the remaining part of this section, all objects of various types, Au disks, Ni and Ag-coated-sphere solid particles, and liquid Sn fragments will all be referred to as *particles* unless specified.

a. Image preprocessing

The image data is preprocessed before passing it to the CNN for training and evaluation. This is done to simplify the data and to remove several properties of the image that do not contain any information about the size of the particle. Firstly, the full-frame images are processed following $\tilde{P}_{ij} = (P_{ij} - P_0)/(P_{b,ij} - P_0)$ where P_{ij} is the raw image of the object and $P_{b,ij}$ is a reference image, containing only the bare illumination. The nonzero parameter P_0 represents the dark noise of the camera. Secondly, each particle is detected, cropped, and centered in the image by a well-tuned detection and centering procedure, combining noise filtering and thresholding steps. Then, as our illumination intensity fluctuates significantly shot to shot, each cropped image is normalized by its own background level, following $\hat{P}_{ij} = P_{ij}/\bar{P}_{ij}$, with \bar{P}_{ij} the center value of a Gaussian fit to the image histogram. After normalization we apply a final crop with a square size of 30 by 30 pixels. Lastly,

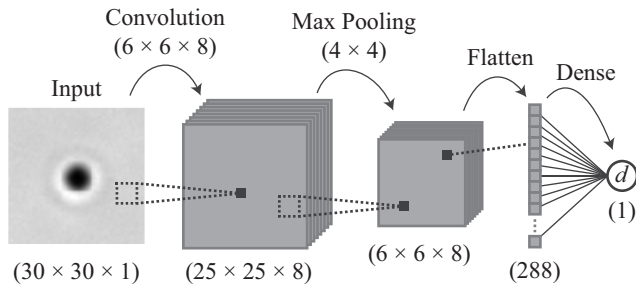


FIG. 11. Diagram of the employed convolutional neural network structure. Data shape for each layer is shown on the bottom. The kernel sizes for each operation is displayed on the top.

for the tin-fragment data, where we have no control over neighboring, close-by objects, a masking step is applied. In this step, all pixels of any object but the most central particle of interest are masked with a value of \bar{P}_{ij} . This allows us to include many more images that would otherwise not give any valid result.

b. Architecture and training

The architecture of the employed network is presented in Fig. 11. The network consists of a single convolutional layer followed by a max-pooling step and a single dense layer after flattening, all with ReLU activation. Minor tuning of the network structure was done using the Ni-particle images as a testing data set. This investigation showed a sensitivity to overfitting for more complex network structures and motivated the use of this, more basic structure. The final employed network is trained on the Au-disk-target images for 2000 epochs with a batch size of 32 and

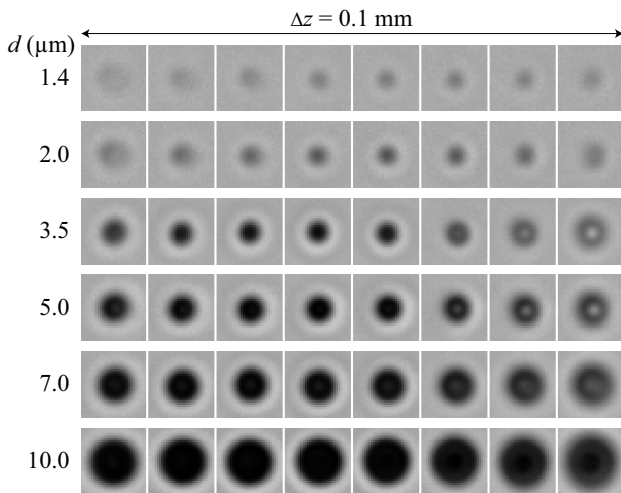


FIG. 12. Selection of Au-disk-target images from the training set. The focal-depth range Δz of the full data set included in the training process spans 0.1 mm in steps of $10 \mu\text{m}$.

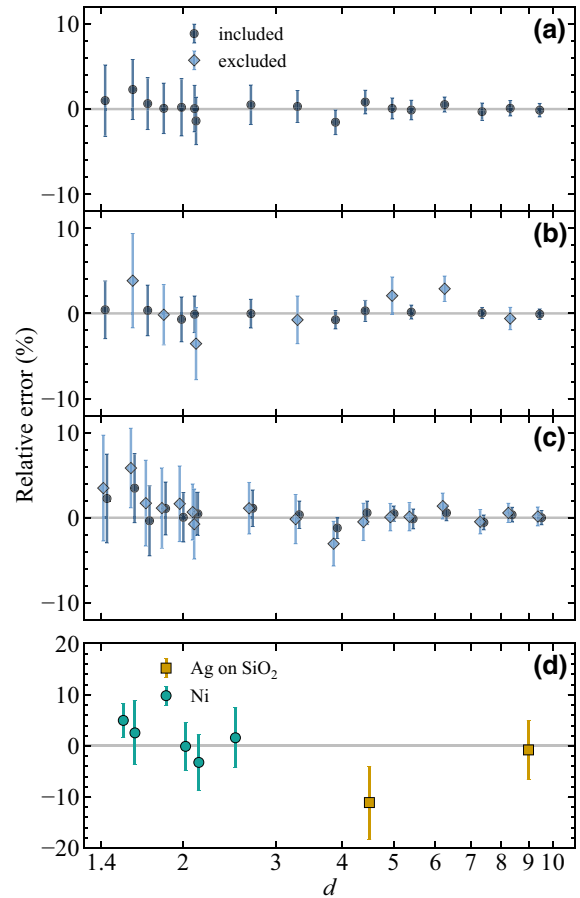


FIG. 13. Relative evaluated size error of (a) the full Au-disk-target training set, (b) a case with random intermediate sizes left out of training, (c) a case where random focal positions are left out of training. In (c) the data markers are slightly horizontally displaced for visual clarity. (d) Overview of the validation-study results, including both the Ni particles and Ag-coated SiO_2 spheres. All data markers and error bars indicate the mean and standard deviation of all included focal positions, respectively.

included a total of 2772 training images. Figure 12 illustrates a selection of these Au-disk training images after preprocessing. The focal-depth range Δz included in the training process spans 0.1 mm in steps of $10 \mu\text{m}$. This range is intentionally chosen to be larger than the accepted focal-depth range of the final evaluated data set (see Sec. III A 2).

Figure 13(a) shows the relative error of the particle diameter of the training data set after training. To test the robustness, i.e., the dependence of the network on specific training input, we perform two test cases where a random selection of sizes or focal positions is left out of training. As can be seen in Figs. 13(b) and 13(c), for both cases comparable evaluation results are obtained for the data excluded from training when compared to Fig. 13(a).

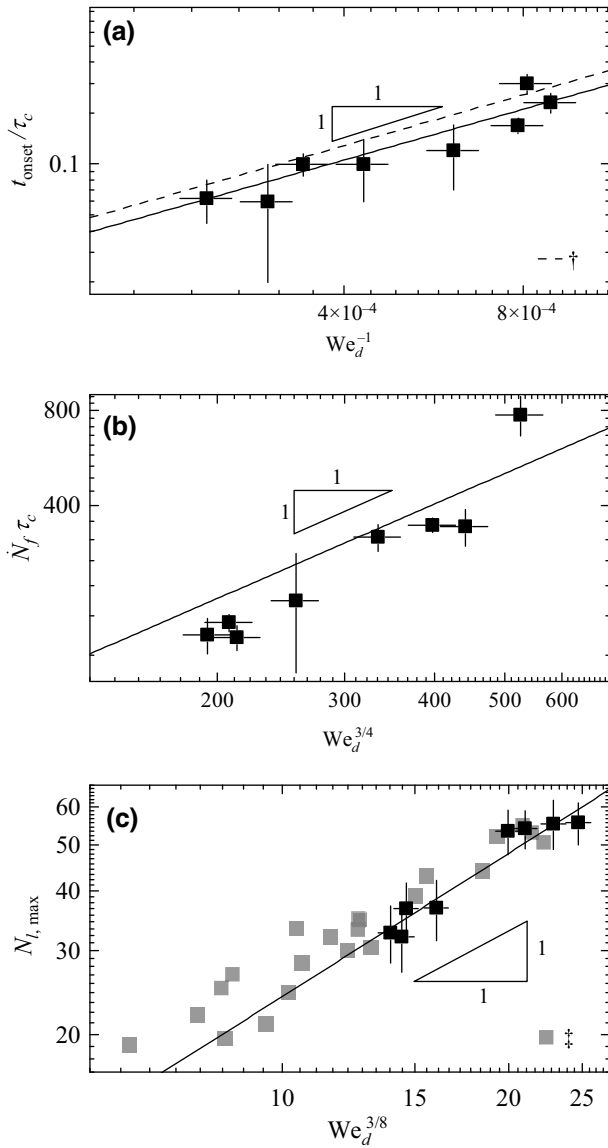


FIG. 14. Linear-linear representations of power-law relation and data from Figs. 2 and 6. Panel (a) presents the scaled onset time of fragmentation t_{onset}/τ_c as a function of We_d^{-1} and the fit from Fig. 2(b); panel (b) shows scaled shedding rate $\dot{N}_f \tau_c$ and the fit from Fig. 2(c) as a function of $We_d^{3/4}$. Panel (c) presents data and the fit from Fig. 6(b) on $N_{l,\text{max}}$ as a function of $We_d^{3/8}$. See the main text for further details.

c. Validation

The physical differences between the Au-disk training targets and spherical tin fragments concern geometry, material, and the presence of a supporting substrate. First, given our plane-wave illumination, we expect no influence of any glass substrate on particle imaging. Furthermore, the limited numerical aperture of our imaging system ($NA = 0.24$) should restrict any possible dependence on the materials' refractive index (for $\lambda = 560$ nm,

Sn: $n + ik = 1.61 + i5.57$ [42], and Au: $0.38 + i2.59$ [43]) and geometry on the diffraction pattern. Refractive-index and shape-related differences in light (Mie) scattering by particles are most prominent at large angles [44,45].

To further strengthen our approach we perform validation studies using two different types of objects: solid Ni particles (Goodfellow, NI00-PD-000119, $n + ik = 1.93 + i3.67$ [46]) and Ag-coated silica spheres (Cospheric, SiO2MS-AG, 100-nm coating thickness, Ag: $0.056 + i3.68$ [43]). These types of particles are mainly chosen because of their availability within our size range of interest.

The Ni particles are deposited on a silica substrate and recorded with our imaging system. As the Ni particles are deposited on a substrate, a systematic focal-depth scan is also performed. The validation data set for these particles includes six focal positions over a 50- μm range. We find that the Ni particles range significantly in size and shape. We therefore investigate them using a scanning electron microscope from which we obtain an accurate, exact size. Particles whose shapes clearly deviate from spherical are discarded.

The Ag-coated silica microspheres, supplied in monodisperse powder form, are sprayed in air and therefore are not supported by any substrate. The recorded images contain many particles at many positions within the focal plane. From these images several particles are picked by manual selection, choosing only those that are close to focus and spatially well isolated. Two particle diameters are used, 4.5 μm (38 particles), and 9 μm (19 particles) with coefficients of variation of 5% each as specified by the manufacturer. As shown in Fig. 13(d) all validation results show a mean size determination error within 10%, which validates the use of Au-disk targets as training objects for evaluation of spherical tin fragments.

2. Linear-linear representation of power-law fits

For clarity the power-law fits and underlying data from Figs. 2 and 6 are here repeated in linear-linear representation, see Fig. 14.

- [1] V. Bakshi, *EUV Lithography* (SPIE Press, Bellingham, 2018).
- [2] Y. Tao, J. T. Stewart, J. Jur, A. LaForge, D. Brown, M. J. Arcand, A. A. Schafgans, and M. A. Purvis, Extreme ultraviolet light source, ASML Netherlands B.V., US Patent 20160007434A1.
- [3] M. Purvis, I. V. Fomenkov, A. A. Schafgans, P. Mayer, K. Hummler, M. H. Leenders, Y. Tao, S. I. Rokitski, J. Stewart, A. I. Ershov, R. J. Rafac, S. D. Dea, G. O. Vaschenko, D. C. Brandt, and D. J. Brown, in *X-Ray Lasers and Coherent X-Ray Sources: Development and Applications XIII*, Vol. 11111, edited by A. Klisnick and C. S. Menoni (SPIE, San Diego, California, USA, 2019).

- [4] O. O. Versolato, Physics of laser-driven tin plasma sources of EUV radiation for nanolithography, *Plasma Sources Sci. Technol.* **28**, 083001 (2019).
- [5] T. Sizyuk and A. Hassanein, Tuning laser wavelength and pulse duration to improve the conversion efficiency and performance of EUV sources for nanolithography, *Phys. Plasmas* **27**, 103507 (2020).
- [6] B. Liu, D. Kurilovich, H. Gelderblom, and O. O. Versolato, Mass Loss from a Stretching Semitransparent Sheet of Liquid Tin, *Phys. Rev. Appl.* **13**, 024035 (2020).
- [7] B. Liu, R. A. Meijer, J. Hernandez-Rueda, D. Kurilovich, Z. Mazzotta, S. Witte, and O. O. Versolato, Laser-induced vaporization of a stretching sheet of liquid tin, *J. Appl. Phys.* **129**, 053302 (2021).
- [8] A. L. Klein, D. Kurilovich, H. Lhuissier, O. O. Versolato, D. Lohse, E. Villermaux, and H. Gelderblom, Drop fragmentation by laser-pulse impact, *J. Fluid Mech.* **893**, A7 (2020).
- [9] B. Liu, J. Hernandez-Rueda, H. Gelderblom, and O. O. Versolato, Speed of fragments ejected by an expanding liquid tin sheet, *Phys. Rev. Fluids* **7**, 083601 (2022).
- [10] F. Torretti, J. Sheil, R. Schupp, M. Basko, M. Bayraktar, R. Meijer, S. Witte, W. Ubachs, R. Hoekstra, O. O. Versolato, A. J. Neukirch, and J. Colgan, Prominent radiative contributions from multiply-excited states in laser-produced tin plasma for nanolithography, *Nat. Commun.* **11**, 1 (2020).
- [11] S. Churilov and A. Ryabtsev, Analysis of the spectra of In XII–XIV and Sn XIII–XV in the far-VUV region, *Opt. Spectrosc.* **101**, 169 (2006).
- [12] G. O’Sullivan, B. Li, R. D’Arcy, P. Dunne, P. Hayden, D. Kilbane, Tom McCormack, H. Ohashi, F. O’Reilly, P. Sheridan, E. Sokell, C. Suzuki, and Takeshi Higashiguchi, Spectroscopy of highly charged ions and its relevance to EUV and soft x-ray source development, *J. Phys. B* **48**, 144025 (2015).
- [13] J. Sheil, O. O. Versolato, A. J. Neukirch, and J. Colgan, Multiply-excited states and their contribution to opacity in CO₂ laser-driven tin-plasma conditions, *J. Phys. B: At. Mol. Opt. Phys.* **54**, 035002 (2021).
- [14] H. Gelderblom, H. Lhuissier, A. L. Klein, W. Bouwhuis, D. Lohse, E. Villermaux, and J. H. Snoeijer, Drop deformation by laser-pulse impact, *J. Fluid Mech.* **794**, 676 (2016).
- [15] E. Villermaux and B. Bossa, Drop fragmentation on impact, *J. Fluid Mech.* **668**, 412 (2011).
- [16] Y. Wang and L. Bourouiba, Growth and breakup of ligaments in unsteady fragmentation, *J. Fluid Mech.* **910**, A39 (2021).
- [17] A. Yarin, DROP IMPACT DYNAMICS: Splashing, Spreading, Receding, Bouncing . . . , *Annu. Rev. Fluid Mech.* **38**, 159 (2006).
- [18] C. Josserand and S. T. Thoroddsen, Drop impact on a solid surface, *Annu. Rev. Fluid Mech.* **48**, 365 (2016).
- [19] G. Riboux and J. M. Gordillo, Experiments of Drops Impacting a Smooth Solid Surface: A Model of the Critical Impact Speed for Drop Splashing, *Phys. Rev. Lett.* **113**, 024507 (2014).
- [20] G. Riboux and J. M. Gordillo, The diameters and velocities of the droplets ejected after splashing, *J. Fluid Mech.* **772**, 630 (2015).
- [21] S. T. Thoroddsen, K. Takehara, and T. G. Etoh, Microsplashing by drop impacts, *J. Fluid Mech.* **706**, 560 (2012).
- [22] A. Rozhkov, B. Prunet-Foch, and M. Vignes-Adler, Dynamics of a liquid lamella resulting from the impact of a water drop on a small target, *Proc. R. Soc. Lond.* **460**, 2681 (2004).
- [23] Y. Wang and L. Bourouiba, Drop impact on small surfaces: Thickness and velocity profiles of the expanding sheet in the air, *J. Fluid Mech.* **814**, 510 (2017).
- [24] J. Eggers, M. Fontelos, C. Josserand, and S. Zaleski, Drop dynamics after impact on a solid wall: Theory and simulations, *Phys. Fluids* **22**, 1063 (2010).
- [25] H. Lastakowski, F. Boyer, A.-L. Biance, C. Pirat, and C. Ybert, Bridging local to global dynamics of drop impact onto solid substrates, *J. Fluid Mech.* **747**, 103 (2014).
- [26] M. Shirota, M. Kato, and A. Ishio, Rim breakups of impacting drops on a superhydrophobic surface and a superheated surface, *Fluids* **7**, 79 (2022).
- [27] Y. Wang and L. Bourouiba, Mass, momentum and energy partitioning in unsteady fragmentation, *J. Fluid Mech.* **935**, A29 (2022).
- [28] A. L. Klein, W. Bouwhuis, C. W. Visser, H. Lhuissier, C. Sun, J. H. Snoeijer, E. Villermaux, D. Lohse, and H. Gelderblom, Drop Shaping by Laser-Pulse Impact, *Phys. Rev. Appl.* **3**, 044018 (2015).
- [29] D. Kurilovich, A. L. Klein, F. Torretti, A. Lassise, R. Hoekstra, W. Ubachs, H. Gelderblom, and O. O. Versolato, Plasma Propulsion of a Metallic Microdroplet and its Deformation upon Laser Impact, *Phys. Rev. Appl.* **6**, 014018 (2016).
- [30] J. Hernandez-Rueda, B. Liu, D. J. Hemminga, Y. Mostafa, R. A. Meijer, D. Kurilovich, M. Basko, H. Gelderblom, J. Sheil, and O. O. Versolato, Early-time hydrodynamic response of a tin droplet driven by laser-produced plasma, *Phys. Rev. Res.* **4**, 013142 (2022).
- [31] M. J. Assael, A. E. Kalyva, K. D. Antoniadis, R. Michael Banish, I. Egry, J. Wu, E. Kaschnitz, and W. A. Wakeham, Reference data for the density and viscosity of liquid copper and liquid tin, *J. Phys. Chem. Ref. Data.* **39**, 033105 (2010).
- [32] J. Lee, W. Shimoda, and T. Tanaka, Surface tension and its temperature coefficient of liquid Sn-X (X=Ag, Cu) alloys, *Mater. Trans.* **45**, 2864 (2004).
- [33] Y. Wang, R. Dandekar, N. Bustos, S. Poulain, and L. Bourouiba, Universal Rim Thickness in Unsteady Sheet Fragmentation, *Phys. Rev. Lett.* **120**, 204503 (2018).
- [34] S. A. Reijers, J. H. Snoeijer, and H. Gelderblom, Droplet deformation by short laser-induced pressure pulses, *J. Fluid Mech.* **828**, 374 (2017).
- [35] R. A. Meijer, D. Kurilovich, K. S. E. Eikema, O. O. Versolato, and S. Witte, The transition from short- to long-timescale pre-pulses: Laser-pulse impact on tin microdroplets, *J. Appl. Phys.* **131**, 105905 (2022).
- [36] P. W. Humrickhouse, An equation of state and compendium of thermophysical properties of liquid tin, a prospective plasma-facing material, *IEEE Trans. Plasma Sci.* **47**, 3374 (2019).
- [37] Y. Wang, Ph.D. thesis, Massachusetts Institute of Technology, 2021.

- [38] L. Wang and Y. Bourouiba, Unsteady sheet fragmentation: droplet sizes and speeds, *J. Fluid Mech.* **848**, 946 (2018).
- [39] R. A. Meijer, Ph.D. thesis, Vrije Universiteit Amsterdam, 2021.
- [40] D. Kurilovich, M. M. Basko, D. A. Kim, F. Torretti, R. Schupp, J. C. Visschers, J. Scheers, R. Hoekstra, W. Ubachs, and O. O. Versolato, Power-law scaling of plasma pressure on laser-ablated tin microdroplets, *Phys. Plasmas* **25**, 012709 (2018).
- [41] T. Gancarz, Z. Moser, W. Gasior, J. Pstrus, and H. Henein, A Comparison of Surface Tension, Viscosity, and Density of Sn and Sn–Ag Alloys Using Different Measurement Techniques, *Int. J. Thermophys.* **32**, 1210 (2011).
- [42] G. Cisneros, J. S. Helman, and C. N. J. Wagner, Dielectric function of liquid tin between 250 and 1100°C, *Phys. Rev. B* **25**, 4248 (1982).
- [43] P. B. Johnson and R. W. Christy, Optical constants of the noble metals, *Phys. Rev. B* **6**, 4370 (1972).
- [44] G. B. J. de Boer, C. de Weerd, D. Thoenes, and H. W. J. Goossens, Laser diffraction spectrometry: Fraunhofer diffraction versus mie scattering, *Part. Part. Syst. Charact.* **4**, 14 (1987).
- [45] G. E. Sommargren and H. J. Weaver, Diffraction of light by an opaque sphere. 1: Description and properties of the diffraction pattern, *Appl. Opt.* **29**, 4646 (1990).
- [46] P. B. Johnson and R. W. Christy, Optical constants of transition metals: Ti, V, Cr, Mn, Fe, Co, Ni, and Pd, *Phys. Rev. B* **9**, 5056 (1974).